



# Ridge-type roughness: from turbulent channel flow to internal combustion engine

Lars H. von Deyn<sup>1</sup> · Marius Schmidt<sup>2</sup> · Ramis Örlü<sup>3,4</sup> · Alexander Stroh<sup>1</sup> · Jochen Kriegseis<sup>1</sup> · Benjamin Böhm<sup>2</sup> · Bettina Frohnappel<sup>1</sup>

Received: 9 July 2021 / Revised: 5 November 2021 / Accepted: 9 November 2021  
© The Author(s) 2021

## Abstract

While existing engineering tools enable us to predict how homogeneous surface roughness alters drag and heat transfer of near-wall turbulent flows to a certain extent, these tools cannot be reliably applied for heterogeneous rough surfaces. Nevertheless, heterogeneous roughness is a key feature of many applications. In the present work we focus on spanwise heterogeneous roughness, which is known to introduce large-scale secondary motions that can strongly alter the near-wall turbulent flow. While these secondary motions are mostly investigated in canonical turbulent shear flows, we show that ridge-type roughness—one of the two widely investigated types of spanwise heterogeneous roughness—also induces secondary motions in the turbulent flow inside a combustion engine. This indicates that large scale secondary motions can also be found in technical flows, which neither represent classical turbulent equilibrium boundary layers nor are in a statistically steady state. In addition, as the first step towards improved drag predictions for heterogeneous rough surfaces, the Reynolds number dependency of the friction factor for ridge-type roughness is presented.

---

✉ Lars H. von Deyn  
von-deyn@kit.edu

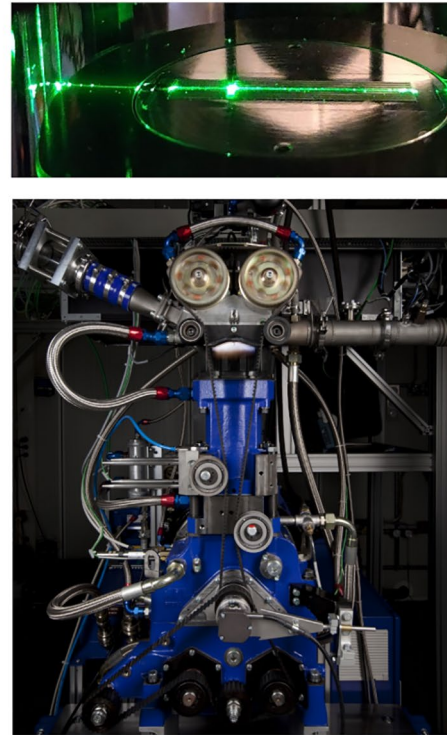
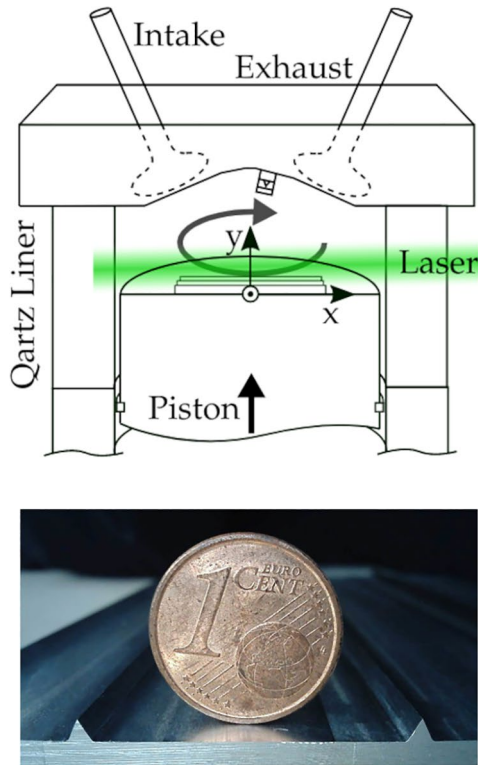
<sup>1</sup> Institute of Fluid Mechanics, Karlsruhe Institute of Technology, Kaiserstraße 10, 76131 Karlsruhe, Germany

<sup>2</sup> Department of Mechanical Engineering, Reactive Flows and Diagnostics, Technical University of Darmstadt, Otto-Berndt-Str. 3, 64287 Darmstadt, Germany

<sup>3</sup> SimEx/FLOW, Engineering Mechanics, KTH Royal Institute of Technology, SE-100 44 Stockholm, Sweden

<sup>4</sup> Mercator Fellow, Karlsruhe Institute of Technology, Karlsruhe, Germany

## Graphic abstract



## 1 Introduction

Predicting the influence of rough surfaces onto turbulent flows is a challenging topic that is of wide interest, ranging e.g. from turbulent boundary layers on aircrafts and ship hulls to atmospheric boundary layers. While engineering tools for the prediction of drag and heat transfer on homogeneous roughness exist, heterogeneous roughness effects are not present in existing predictive frameworks (Chung et al. 2021).

Nevertheless, inhomogeneous roughness is a key feature of many environmental and engineering surfaces (Colombini and Parker 1995; Mejia-Alvarez and Christensen 2013; Bons et al. 2001). The present work focuses on spanwise heterogeneous roughness in which streamwise strips of roughness (or models thereof) alternate with smooth wall strips.

Such surfaces are known to produce secondary motions of the Prandtl's second kind that can spatially extend through the entire boundary-layer thickness. These vortical secondary motions are found in the temporally averaged flow field in the cross plane perpendicular to the mean flow direction and only amount to a few percent of the main flow's kinetic energy. Despite this relatively weak intensity they

can strongly alter the mean flow field, and, in consequence, the drag and heat transfer properties of a turbulent boundary layer (see e.g. Stroh et al. 2019).

In the literature, two simplified configurations of spanwise inhomogeneous roughness are often distinguished, strip-type and ridge-type roughness. In case of strip-type roughness it is assumed that the boundary-layer thickness is much larger than the characteristic scale of the roughness height, such that the roughness elevation can be neglected. This simplification can be exploited in numerical simulations in which a spanwise alternating wall-shear stress is prescribed on a geometrically smooth wall (Anderson et al. 2015; Chung et al. 2018). For ridge-type roughness, in contrast, the elevation difference between rough and smooth surface is in focus. Alternating rough and smooth strips are simplified to smooth protruding ridges aligned in streamwise direction on a smooth wall, see e.g. Medjnoun et al. (2018); Hwang and Lee (2018).

Both simplified surface configurations generate secondary motions of the Prandtl's second kind when exposed to a turbulent shear flow oriented in direction of the roughness strips. In case of the strip-type roughness the secondary motion produces a downwelling motion over the region

of higher wall-shear stress (Hinze 1967), while in case of ridge-type roughness an upwelling motion is detected over the protruding ridges (Vanderwel and Ganapathisubramani 2015). It was shown by Stroh et al. (2020) that real roughness strips can yield secondary motions that are either very similar to the ones above ridge-type roughness or to the ones above strip-type roughness, depending on the relative surface elevation of the roughness. From the view point of the generated secondary motion, a protruding deposition-type roughness was found to resemble ridge-type roughness while a recessed corrosion type roughness is similar to strip-type roughness. A strip-type roughness configuration was recently studied experimentally by Wangsawijaya et al. (2020) confirming the results of numerical studies of real roughness (Stroh et al. 2020) and spanwise alternating slip (Chung et al. 2018).

Investigations in this field date back to the work of Hinze (1967) and are mostly based on canonical wall bounded shear flow configurations (turbulent duct, channel and boundary layer flows). For these equilibrium boundary layer flow conditions there is a wide range of recent investigations, including e.g. the temporal dynamics of the secondary motions (Wangsawijaya et al. 2020) or the link between secondary flows and very large scale motions (Zampiron et al. 2020).

However, the more recent interest in this topic was spiked by the discovery by Bons (2002) that drag and heat transfer on realistically rough gas turbine blades differed from predictions based on data from homogeneous rough surfaces. In addition, literature provides indications of the robustness of the secondary flow formation in the sense that they do not necessarily require the streamwise homogeneity characteristic for strip-type or ridge-type roughness. In fact, the occurrence of secondary motions was also reported for turbulent flows over elliptical roughness spots (Mejia-Alvarez and Christensen 2013) or irregular rough surfaces with clustered roughness elements (Womack et al. 2019). It is thus interesting to understand whether the presence of heterogeneous roughness in certain complex flows, that do not resemble the classical canonical flow states, also leads to the formation of large-scale secondary motions.

In the present work we focus on ridge-type roughness as one of the simplified models for spanwise inhomogeneous roughness. The corresponding secondary motion is first described in detail for fully developed turbulent channel flow configurations at different Reynolds numbers using Direct Numerical Simulations (DNS) as well as complementary experimental approaches, namely hot-wire (HW) anemometry and stereoscopic Particle Image Velocimetry (sPIV).

In the second step the investigated ridge-type geometries are transferred onto the piston of an optically accessible engine. During the compression stroke of the engine, a boundary layer develops along this piston. Based on planar

Particle Tracking Velocimetry (PTV) measurements we aim to understand whether this non-equilibrium turbulent boundary layer can be influenced through streamwise ridges in a qualitatively similar manner than observed for the turbulent channel flow, thus providing evidence for the formation of secondary flow structures under engine operating flow conditions.

While the presence of secondary flows in the engine boundary layer is of interest by itself, the related changes in drag and heat transfer are critical for the evaluation of the potential relevance of secondary motions for combustion processes. However, existing engineering tools cannot capture these effects. The available predictive tools rely on the use of an equivalent sand grain roughness and Reynolds analogy factor that are evaluated for homogeneous rough surfaces (see e.g. Chung et al. 2021; Forooghi et al. 2017, for more details). As the first step towards the inclusion of spanwise inhomogeneous roughness effects into predictive engineering tools, the Reynolds number dependency of the friction factor, which corresponds to the classical Nikuradse diagram, needs to be available. Based on pressure drop measurements of a turbulent channel flow with ridge-type roughness over a wide Reynolds number range such data is presented for ridge-type roughness for the first time.

## 2 Investigated geometries

We consider ridge-type roughness in the form of streamwise aligned ridges with rectangular ( $\square$ ) and triangular ( $\triangle$ ) cross section. Ridges with rectangular cross section are the most widely investigated literature case, while ridges with triangular cross section are known to induce stronger secondary motions for the same cross sectional area of the ridge (Stroh et al. 2019; Medjnoun et al. 2020).

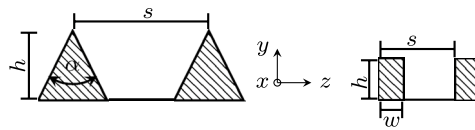
A summary of all conducted experiments and simulations for the present investigation is given in Table 1. From the available literature, it is expected that in the chosen range of wavelength  $s/\delta$  and structure height  $h/\delta$  a pronounced secondary motion is evident in turbulent shear flows Medjnoun et al. (2020); Vanderwel and Ganapathisubramani (2015).

In general, as can be seen from Table 1, comparable wavelengths  $s/\delta$  between channel ( $\triangle : s/\delta = 2.16$ ,  $\square : s/\delta = 1.22$ ) and piston ( $\triangle : s/\delta = 1.52$ ,  $\square : s/\delta = 1.12$ ) are chosen while the structure height  $h/\delta$  differs. Here,  $\delta$  refers to the boundary-layer thickness or the channel half-height, respectively. From the literature, a strong secondary motion is expected for  $s/\delta \approx 1$  (Vanderwel and Ganapathisubramani 2015; Yang and Anderson 2018). This spacing is applied for the rectangular structures. Two times larger  $h/\delta$  is deliberately chosen for the triangular structures (channel:  $0.158 h/\delta$  vs.  $0.078 h/\delta$ ) to increase the strength of the secondary motions. At the same time  $s/\delta$

**Table 1** Overview of the investigated ridge-type roughness surfaces;  $\delta$  refers to the channel half-height (12.60mm) and to the  $\delta_{99}$  boundary-layer thickness in the engine (0.89mm), respectively. For the dimensions of the surface ridges the normalized average value and

the maximum measured variation is given. The bulk Reynolds number  $Re_b$  is included to quantify the global flow state. Note that  $Re_b$  is defined differently in case of channel (see section 3.1) and piston flow (see section 4.1)

ID	flow type	data source	$s/\delta$	$h/\delta$	$\alpha$ [°]	$w/\delta$	$Re_b$
refpiston	engine	PTV					$1.5 \times 10^4$
refdns	channel	DNS					$1.8 \times 10^4$
tridpdx	channel	$\Delta p$	$2.16 \pm 0.09\%$	$0.158 \pm 0.13\%$	$54.8 \pm 0.91\%$		$(0.5 - 8.5) \times 10^4$
trihw12	channel	HW	$2.16 \pm 0.09\%$	$0.158 \pm 0.13\%$	$54.8 \pm 0.91\%$		$1.2 \times 10^4$
trihw18	channel	HW	$2.16 \pm 0.09\%$	$0.158 \pm 0.13\%$	$54.8 \pm 0.91\%$		$1.79 \times 10^4$
trihw37	channel	HW	$2.16 \pm 0.09\%$	$0.158 \pm 0.13\%$	$54.8 \pm 0.91\%$		$3.75 \times 10^4$
trihw58	channel	HW	$2.16 \pm 0.09\%$	$0.158 \pm 0.13\%$	$54.8 \pm 0.91\%$		$5.82 \times 10^4$
tridns	channel	DNS	2.16	0.158	54.8		$1.8 \times 10^4$
tripiv	channel	sPIV	$2.16 \pm 0.09\%$	$0.158 \pm 0.13\%$	$54.8 \pm 0.91\%$		$1.8 \times 10^4$
tripiston	engine	PTV	$1.52 \pm 0.66\%$	$0.376 \pm 9.04\%$	$65 \pm 3.07\%$		$1.5 \times 10^4$
rectpdx	channel	$\Delta p$	$1.22 \pm 0.57\%$	$0.078 \pm 1.92\%$		$0.238 \pm 0.84\%$	$(0.5 - 8.5) \times 10^4$
recthw	channel	HW	$1.22 \pm 0.57\%$	$0.078 \pm 1.92\%$		$0.238 \pm 0.84\%$	$1.8 \times 10^4$
rectdns	channel	DNS	1.22	0.078		0.238	$1.8 \times 10^4$
rectpiston	engine	PTV	$1.12 \pm 0.89\%$	$0.174 \pm 19.54\%$		$0.562 \pm 0.18\%$	$1.5 \times 10^4$



is increased to keep the blockage effects similar. Since the boundary-layer thickness over the engine piston amounts to less than 10% of the half-channel height, an approximately two times larger  $h/\delta$  ( $\Delta$ : 0.378 for engine vs. 0.158 channel flow) had to be chosen due to manufacturing limitations. Since the surface on the piston onto which structures can be inserted is limited (see Sect. 4.2),  $s/\delta$  is constrained to  $s/\delta = 1.52$  for the engine experiment such that at least 9 parallel ridge structures can be accommodated on the piston. The presented configurations are deemed to be the best compromise between these competing effects.

The last column of Table 1 reports the bulk Reynolds number  $Re_b$ , which is included to describe the general operating condition of the experiments. Note that the bulk Reynolds number definition between channel and engine flow differ (see Sects. 3.1 and 4.1 for details) such that the similar magnitudes reported here do not necessarily reflect similar flow dynamics.

### 3 Ridge-type roughness in turbulent channel flow

The secondary motion over ridges with rectangular and triangular cross section and its impact on the streamwise mean velocity profile is investigated in the classical turbulent channel-flow configuration in terms of DNS of a plane channel configuration and experiments in a channel (duct) of aspect ratio 1:12. The corresponding governing equations as well as experimental and numerical procedures are described in the following.

#### 3.1 Governing equations and problem description

The governing equations are the continuity and Navier-Stokes equations for the incompressible flow of a Newtonian fluid

$$\frac{\partial u_i}{\partial x_i} = 0, \quad (1)$$

$$\frac{\partial u_i}{\partial t} + u_j \frac{\partial u_i}{\partial x_j} = -\frac{1}{\rho} \frac{\partial p}{\partial x_i} + \nu \frac{\partial u_i}{\partial x_j \partial x_j} + F_i, \quad (2)$$

with the three velocity components  $(u_1, u_2, u_3) = (u, v, w)$  (along the streamwise, wall-normal and spanwise  $(x_1, x_2, x_3) = (x, y, z)$ -axes, respectively).  $F_i$  denotes a force (per unit mass) used for numerical purposes as discussed in Sect. 3.3. For fully developed turbulent flow, the wall friction  $\tau_w$  can be derived from the streamwise pressure gradient  $\Pi = \frac{\partial p}{\partial x}$  via  $\tau_w = -\delta\Pi$ , where  $\delta$  corresponds to the net channel half-height (see below). This relation is used in the experimental procedure (see Sect. 3.2) to obtain the skin-friction coefficient

$$C_f = \frac{2\tau_w}{\rho U_b^2}, \quad (3)$$

with  $U_b$  being the bulk velocity (volume flow rate normalized by channel cross section), also used for the formulation of the bulk Reynolds number  $Re_b = \frac{2U_b\delta}{\nu}$ . Additionally, based on  $\tau_w$ , the friction velocity  $u_\tau = \sqrt{\frac{\tau_w}{\rho}}$  and the respective friction Reynolds number  $Re_\tau = \frac{u_\tau\delta}{\nu}$  is obtained. Throughout the manuscript, the superscript  $+$  refers to viscous units, i.e. a normalization based on  $u_\tau$  and the kinematic viscosity  $\nu$ .

One rectangular and one triangular ridge configuration are each complementarily investigated at  $Re_b = 1.8 \times 10^4$ , employing DNS of a doubly-periodic turbulent channel flow (i.e. of infinite extend) along with HW and sPIV measurements in turbulent channel (duct) flow of aspect ratio 1:12. Pressure-drop measurements are conducted for the whole measuring range of the experimental channel-flow facility up to  $Re_b = 8.5 \times 10^4$  (see Sect. 5). Additional hot-wire measurements are carried out to study Reynolds number effects up to  $Re_b = 5.82 \times 10^4$  for triangular ridges only.

For the channel flow experiment, the investigated triangular and rectangular ridge geometries were milled with a high precision CNC milling-machine. A section extending  $119\delta$  in the streamwise direction was equipped with the surface structures. The net half-channel height, defined as the distance from the surface structures average (melt-down) height up to the channel centerline, is chosen to match the smooth reference value of  $\delta = 12.60$  mm. In doing so, the net fluid volume in the channel is kept identical between different cases. The geometrical parameters stated in Table 1 were verified via optical (Sensofar S neox<sup>®</sup>) and tactile measurements (perthometer Mahr MarSurf PCV<sup>®</sup>). The detected deviations which stem from the manufacturing process are included as percentage uncertainties.

### 3.2 Experimental methods

The experimental investigations are carried out in an open-circuit blower tunnel (Güttler 2015). It allows the measurement of small changes in skin-friction drag by evaluating the static pressure at 21 pressure taps located along both

side walls of a  $314\delta$  long channel test section with an aspect ratio of 1:12 and hot-wire measurements at the downstream end of the test section. The test section is divided into three segments of  $76\delta$ ,  $119\delta$  and  $119\delta$  streamwise extents. In the present investigation the last segment is equipped with 19 rectangular or 10 triangular elevated streamwise-aligned ridges symmetrically arranged on the upper and lower side of the test section with the characteristics shown in Table 1. The facility allows to vary the bulk Reynolds number in the range of  $5 \times 10^3 < Re_b < 8.5 \times 10^4$ .

The streamwise pressure gradient  $\Pi$  assessed via the 0.3 mm static pressure taps spaced 200 mm in streamwise direction is required to evaluate the global wall-shear stress  $\tau_w$  as described in Sect. 3.1.

For this purpose, a MKS Baratron 698A unidirectional differential pressure transducer with 1333Pa maximum range and an accuracy of 0.13% of the reading is employed. In combination with the flow rate  $\dot{V}$ , measured with an orifice flow meter with interchangeable orifice plates, the skin friction coefficient  $C_f$  defined through eq. (3) can be deduced. The orifice's pressure drop is measured with one of two Setra 239D (125Pa and 625Pa full-scale) unidirectional differential pressure transducers with an accuracy of 0.07% of the full-scale, switching automatically depending on  $Re_b$ . Changes in ambient conditions are accounted for by tracking the systems inlet and outlet temperature via PT100 thermocouples and the ambient pressure and humidity using Adafruit BMP 388 and BME 280 sensors, respectively. Details of this procedure are described in Gatti et al. (2020).

In addition, a hot-wire probe is used to measure the streamwise velocity at different wall-normal and spanwise positions. The streamwise location of the measurement campaign was fixed to one centimeter upstream of the test-section outlet, since measurements showed that the first- and second-order statistics were identical with those measured up to 15cm upstream of test-section outlet. The probe consists of a single hot-wire probe of boundary-layer type (replicating a DANTEC 55P15) with a  $2.5\mu\text{m}$  diameter Platinum wire and a sensing length of about 0.5mm, resulting in an inner-scaled wire length of  $L^+ \approx 20$  at a friction Reynolds number of  $Re_\tau \approx 550$ . This length was deemed sufficient to adequately resolve the turbulence statistics (Hutchins et al. 2009).

A DANTEC Streamline Pro frame in conjunction with a 90C10 constant temperature anemometer (CTA) system is used and operated at fixed overheat ratio of 80%. The velocity calibrations for the hot wires were performed ex situ in an external high contraction ratio jet facility, while mean temperature changes during the runs were limited to  $< 2$  K and could therefore be compensated as outlined by Örlü and Vinuesa (2017). Turbulence statistics were acquired with a sampling time between 10s and 60s and an acquisition frequency of 60kHz, depending on  $Re_b$ . An offset and gain



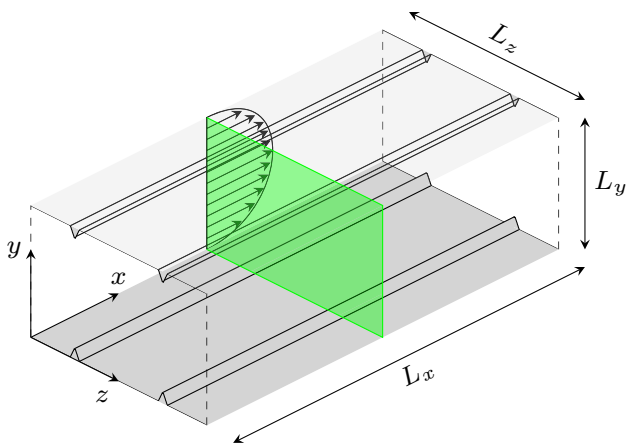


**Fig. 1** Schematic of investigated channel-flow configuration including ridge geometry.  $L_x, L_y, L_z$  denote the DNS simulation domain dimensions (Table 2). Green plane indicates the laser-light sheet for the sPIV measurements

was applied to the top of the bridge voltage in order to match the voltage range of the 16-bit A/D converter used. In order to avoid aliasing at the higher velocities, an in-built analog low-pass filter was set up at the Nyquist frequency prior to data acquisition.

Measurements were conducted with an automated traversing system acquiring wall-normal velocity profiles at 39 positions in log-spacing above the ridge crest and the ridge valleys, respectively ( $y$ -direction, see Fig. 1). Additionally, 2D scans consisting of 1110 measurement points in the spanwise and wall-normal direction were carried out ( $z$ - $y$ -plane). The 30 measurement points in spanwise direction were spaced equidistantly in the valley and refined at the ridge, while 37 wall-normal locations were spaced logarithmically.

In order to resolve the wall-normal and spanwise velocity components, complementary sPIV measurements were carried out. For this purpose, an additional test section identical in its dimensions to the one used for pressure drop and hot wire measurements was employed. This test section allows the use of optical particle-based measurement techniques. As the two test sections are of identical dimensions, the exact same sets of streamwise aligned ridges were measured with sPIV as for pressure-drop and hot-wire experiments.

The measurement plane captured a cross section of the flow  $3.5 \delta$  upstream of the test-section outlet. Its orientation with respect to the ridges is visualized in Fig. 1. Two Photron SA4 high-speed cameras at the left and right side of the channel exit, positioned at approximately  $28^\circ$  with respect to the streamwise direction, were used to take particle images, avoiding flow blockage. The lenses with a focal length of 200mm and an aperture of  $f/8$  were used in conjunction with a tele converter for each lens and mounted on Scheimpflug adapters fitted to accommodate the oblique viewing angles. The cameras were operated in double-frame mode (sampling

frequency 480 Hz) at full sensor size ( $1024 \times 1024$  px) and a spatial resolution of about 60 px/mm. The particles were illuminated by a Quantronix Darwin-Duo Nd:YLF laser that accesses the channel test section through a convex lens window, used to parallelize the light sheet to the wall, thus minimizing reflection issues from the walls. The light sheet thickness was set to 0.5mm corresponding to  $\approx 30$  px. A laser pulse distance of 12ms (repetition rate 240Hz) was adopted for  $Re_b = 1.8 \times 10^4$  to reach the desired 10 px displacement in streamwise direction.

PIVview software was used to process the particle images in a multigrid/multipass approach, where the raw images were cross-correlated on a final interrogation window size of  $48 \times 16$  px with an overlap factor of 50%. Spurious vectors (1.9%) were removed with a normalized median test (threshold 3) as proposed by Westerweel and Scarano (2005). An averaged background image subtraction was used to avoid reflection issues in the first interrogation area closest to the wall. Further details on the experimental set-up are provided by Hehner et al. (2021b, 2021a).

### 3.3 Numerical method

DNS of a fully developed turbulent channel flow in a smooth and structured configuration replicating the experiment were carried out under constant flow-rate conditions. The code implementation is based on the pseudo-spectral solver with Fourier expansions in the streamwise ( $x$ ) and spanwise ( $z$ ) directions and Chebyshev polynomials in the wall-normal direction ( $y$ ) (see Chevalier et al. 2007). Periodic boundary conditions are employed in streamwise and spanwise directions such that in contrast to the experiment the DNS set-up does not contain any side walls. The required surface structuring is implemented with an immersed boundary method (IBM) according to Goldstein et al. (1993). The method imposes zero velocity in the solid region of the numerical domain utilizing a volume force distribution  $F_i$  which is added to the Navier-Stokes equations (eq. (2)) at every time instant of the simulation. This IBM implementation was validated for rough surfaces by Forooghi et al. (2018) and has successfully been used in previous works on secondary motions generated through longitudinal ribs (Stroh et al. 2019; Castro et al. 2021).

Details about the simulation domain and resolution for the present cases are presented in Table 2. For all cases a fixed resolution of  $N_x \times N_y \times N_z = 768 \times 385 \times 384$  grid points was used. The spanwise simulation domain extent is adjusted to accommodate an integer amount of structure wavelengths  $s/\delta$  in the computational box. Temporal and spatial averaging in the streamwise direction is applied to the DNS results, since the secondary motion is observed in the cross-sectional plane perpendicular to the main flow direction. The transient of the simulation was excluded from

**Table 2** Simulation domain properties

ID	$Re_b$	$L_x \times L_y \times L_z$		
refdns	$1.8 \times 10^4$	$8\delta \times 2\delta \times 4\delta$		
tridns	$1.8 \times 10^4$	$8\delta \times 2\delta \times 4.32\delta$		
rectdns	$1.8 \times 10^4$	$8\delta \times 2\delta \times 3.66\delta$		
ID	$\Delta x^+$	$\Delta y_{min}^+$	$\Delta y_{max}^+$	$\Delta z^+$
refdns	5.16	0.017	4.05	5.16
tridns	5.66	0.018	4.44	6.16
rectdns	5.66	0.018	4.44	5.26

time averaging, leaving at least 100 flow-through times for temporal averaging. The bulk Reynolds number  $Re_b$  for the comparison of hot-wire and sPIV results to numerical data is set to  $Re_b = 1.8 \times 10^4$ , which corresponds to a friction Reynolds number of  $Re_\tau \approx 500$  in the smooth-wall case.

### 3.4 Secondary flow

The studied ridge configurations listed in Table 1 induce a pronounced secondary flow detectable in the time-averaged cross-plane velocity components  $V$  and  $W$ . The measured and simulated magnitudes  $\sqrt{V^2 + W^2}/U_0$  in proximity of the triangular ridges are compared in Fig. 2, where the sPIV has been recorded at the spanwise channel center.  $\sqrt{V^2 + W^2}$  is normalized with the global centerline velocity  $U_0$ , derived from the spanwise averaged velocity profile. In the ridge vicinity, a significant secondary motion magnitude up to 4.5% is evident, caused by a domain-filling counter rotating vortex pair (black vectors in Fig. 2). In the  $\delta \times \delta$  sized field of view of the sPIV experiment, very good agreement with the DNS results is found indicating that the spanwise periodicity of the DNS does not induce any significant differences in the generated secondary flow compared to the duct flow of aspect ratio 1:12 in the experiment.

The secondary flow has a distinct effect on the mean streamwise velocity  $U$ , as can be observed in Fig. 3. The iso-lines of  $U$  obtained by hot-wire measurements and DNS show a strong spanwise variation and pronounced bulging effect above the ridge.

The wall-distance of the first hot-wire measurement point is not known a priori (Örlü et al. 2010). Thus, from the 2D hot-wire measurement grid, the mid valley velocity profile between two ridges is fitted against a law of the wall proposed by Luchini (2018). In doing so,  $u_\tau$  and the wall distance of the first measurement point  $y_0$  closest to the wall is determined (only  $y_0$  is used in the following since the velocity profiles are shown in outer scaling). This approach implies a velocity profile in the structure’s valley of the same

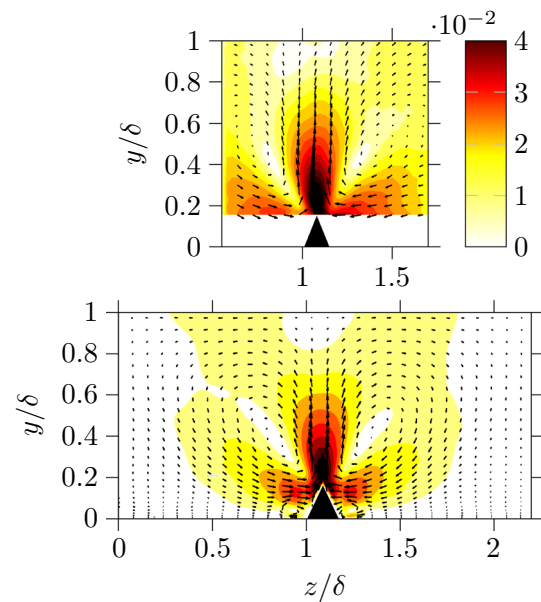


**Fig. 2** Secondary motion magnitude  $\sqrt{V^2 + W^2}/U_0$  contours for sPIV (top) and DNS (bottom) at  $Re_b = 1.8 \times 10^4$ . The direction of the secondary motion is represented by arrows

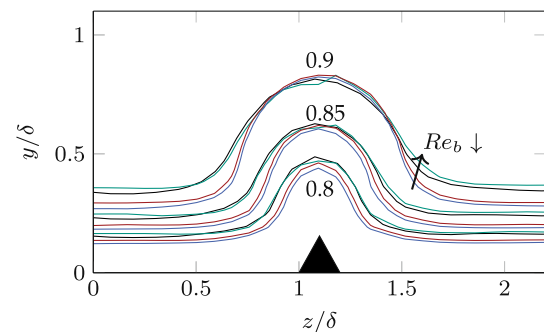


**Fig. 3** Contours of mean streamwise velocity  $U/U_0$ . Green (hot wire):  $Re_b = 1.2 \times 10^4$ . Black (DNS):  $Re_b = 1.8 \times 10^4$ . Red (hot wire):  $Re_b = 3.7 \times 10^4$ . Blue (hot wire):  $Re_b = 5.8 \times 10^4$

shape as in the smooth reference case which leads to good agreement with the DNS, justifying the assumptions made (see Fig. 5, left).

Again, very good agreement between the experimental and numerical results is found, indicating that the limited channel width of the experiment does not modify the effect of the secondary motion on the streamwise mean flow. The fact that the secondary flow is not confined to the ridge vicinity, as already observed in Fig. 2, also reflects in the bulging of  $U$  up to the channel center. Therefore, outer-layer similarity, typically encountered above homogeneous rough surfaces (Chung et al. 2021), does not hold for this type of heterogeneous roughness.

Note that only a weak Reynolds number dependence of the bulging effect can be observed, which is consistent with previous studies (cf. e.g. Vanderwel et al. 2019). For increasing  $Re_b$ , the iso-lines tend to be slightly closer to the wall in the ridge valley. However, overall the results in Fig. 3 indicate a robust behavior of the secondary motion, largely independent of  $Re_b$ .

In consequence, it is hypothesized that similar effects of these surface structures on the turbulent flow likewise occur in internal combustion (IC) engines, at least during parts of the engine cycle for which wall-parallel flow is present in this highly complex flow. This will be thoroughly elaborated in the following section.

## 4 Ridge-type roughness in internal combustion (IC) engine

### 4.1 Piston boundary layer

Engine geometries such as the intake port and valve shapes are designed to produce a large-scale rotational flow motion called tumble. Its rotational axis ( $\parallel z$ , see Fig. 4) is aligned perpendicular to both the cylinder axis ( $y$ ) and the symmetry plane bisecting the two intake and exhaust valves, respectively (in a four valve engine). Consequently, this bisecting symmetry plane, in which the rotation of the tumble occurs, is called the tumble plane. In a four stroke engine, air is first inducted in the intake stroke, then compressed in the compression stroke. The fuel-air mixture of a spark-ignition (SI) engine is ignited, which leads to the combustion or expansion stroke. Finally the exhaust stroke expels the burnt gases, concluding one engine cycle. The purpose of the large scale tumble motion common in SI-engines is to store rotational energy to assist the fuel-air mixing or (post-) combustion processes later in the cycle (Borée and Miles 2014).

When phase-averaging this cyclic, unsteady flow, i.e. averaging many cycles at a fixed crank angle degree and therefore piston position, a repeatable flow field emerges. However, the flow of an individual cycle is not only highly turbulent, but also affected by significant cycle-to-cycle variations (CCV) of large scale flow structures. Of course this complex 3D-flow interacts heavily with the surrounding walls, such as the valves, cylinder liner and piston walls, in the form of wall jets, detachments and parallel flows. During compression, the tumble motion leads to an average flow in the tumble plane, which is piston-wall parallel if observed in a piston-relative frame. Compared to canonical channel flows, the boundary layer is less developed and locally subject to adverse pressure gradients. Furthermore, due to the compression, gas properties such as density and viscosity change in time. Even in motored operation (without ignition)

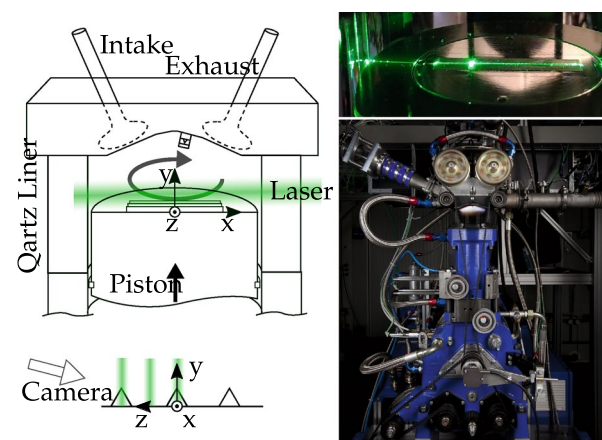


**Fig. 4** Left: Schematic of IC engine experiment. Green planes represent PTV measurement planes with respect to the ridge position. An arrow indicates the rotational tumble motion. Right top: Structured piston with laser light sheet. Right bottom: Overview picture of the optical engine

this leads to a significant temperature gradient and heat transfer between the gas and the wall.

Studying near-wall flows in an engine environment experimentally is challenging due to the high resolution requirements and the difficulty in distinguishing between turbulent fluctuations and cyclic variations. Alharbi and Sick (2010) resolved the boundary layer at the cylinder head of a motored engine. In the same configuration Jain-ski et al. (2012) reported the absence of a logarithmic layer, a finding which was replicated for other configurations by Renaud et al. (2018) and Shimura et al. (2018). Ma et al. (2016) evaluated the performance of classical wall-models used in numerical simulations and proposed a model for zonal simulations. MacDonald et al. (2017) investigated the turbulent fluctuations in the boundary layer and the contributions from the core flow and the wall shear. High-fidelity simulations of engine flows are not limited to certain locations and time instances, as are experiments, but are computationally expensive and only few have been published so far: Schmitt et al. (2015) studied velocity and temperature boundary layers in a simplified numerical configuration with a weak bulk flow and reported self similarity of scaled profiles when taking the local fluid properties into account.

The velocity boundary layers above the piston of the Darmstadt engine, used in the current work, have been studied by Renaud et al. (2018). For 800rpm, an intake pressure of 0.95bar, and at  $-60^\circ\text{CA}$  (degree crank angle after ignition top dead center) the global Reynolds number  $Re_b$  is  $1.5 \times 10^4$ , when defined by mean piston speed, bulk viscosity, and bore size. They found velocity boundary layers with Reynolds numbers based on the momentum thickness  $Re_{\delta_*}$



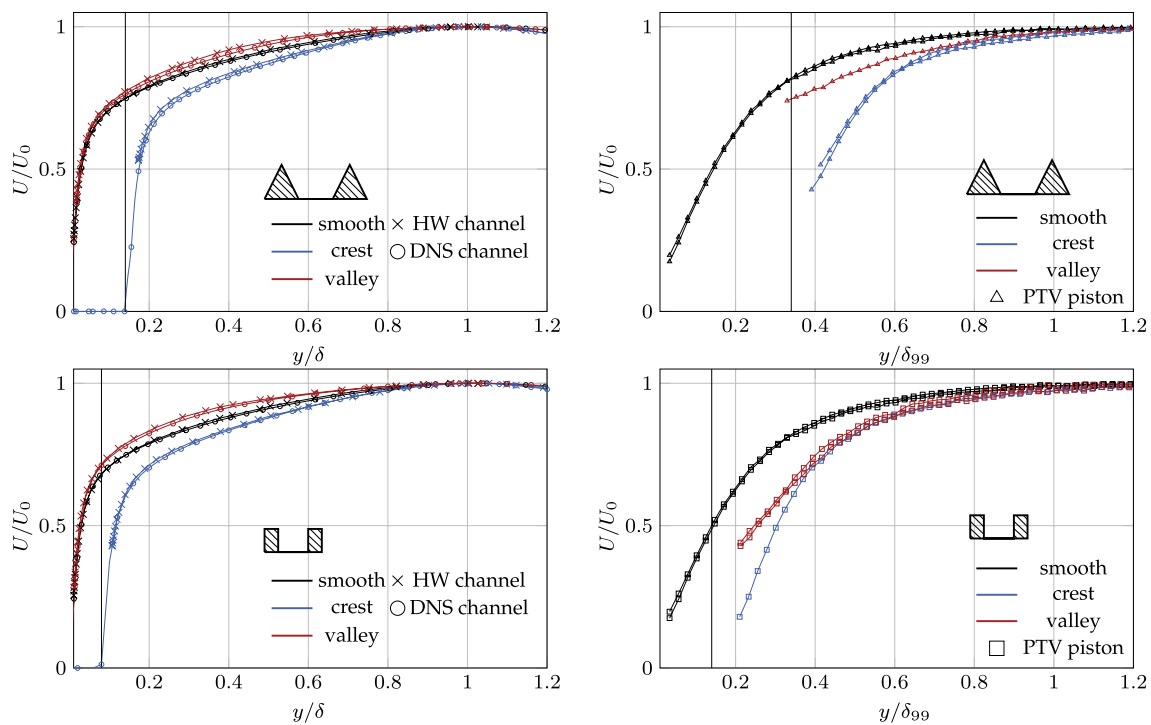


**Fig. 5** Comparison of streamwise velocity  $U$  vs.  $y$  for triangular (top) and rectangular (bottom) structures in channel and IC engine flow. Left: structured channel. Right: structured piston. DNS and HW (channel) scaled with the local centerline velocity  $U_0$  and half channel height  $\delta$ . DNS and HW measured at  $Re_b = 1.8 \times 10^4$ . PTV (IC

engine) data are made dimensionless with the respective maximal velocity and the wall-normal position  $\delta_{99}$  of the reference measurement. The black vertical lines represent the ridge height  $h/\delta$  of each case

being lower than 100, with the asterisk signifying *semi-locally* scaled values, that take the temperature boundary layer into account (see e.g. Schmitt et al. 2015). The displacement thickness  $\delta_1^*$  amounted to roughly 0.2mm and the boundary-layer thickness  $\delta_{99}$  was found to be 0.89mm. Here,  $\delta_{99}$  refers to the location at which 99% of the maximum time-averaged wall-parallel velocity is reached. In the engine flow, the wall-parallel velocity increases in the boundary layer with increasing wall distance, reaches a maximum and decreases again due to the presence of the tumble vortex. It is noteworthy that  $\delta_{99}$  is an experimentally sensitive value, especially in this context of engine flows. It is nevertheless used as reference length scale for the present investigation since it is known to be a relevant scale for the formation of secondary flows in canonical boundary layers over heterogeneous rough surfaces.

In the current work, surface structures were applied to the piston top to investigate whether a ridge-type roughness leads to the formation of large-scale secondary motions in the piston velocity boundary layer during the operating conditions described above. In the central piston region investigated, the flow is on average wall-parallel and can be considered quasi two-dimensional, since variations in the

spanwise ( $z$ -) direction and the average spanwise velocity component  $w$  are small.

### 4.2 Experimental set-up

Measurements were performed in the Darmstadt Engine, a four-stroke single-cylinder spark ignition optical research engine at the Technische Universität Darmstadt. Its four-valve spray-guided pent-roof cylinder head features a compression ratio of 8.7:1 with a bore and stroke of 86mm each. A fused-silica cylinder liner offers optical access in the top 55mm of the stroke and an additional 8mm in the pent-roof. Detailed information about the engine and its periphery has already been reported by Freudenhammer et al. (2015) and Baum et al. (2014). The engine was operated at 800rpm at an intake pressure of 0.95bar such that  $Re_b = 1.5 \times 10^4$ .

Triangular and rectangular ridge geometries were applied to the piston top by means of an aluminium insert in place of the usual quartz glass window. A total of nine ridges with a length of 40mm each, were milled with a CNC milling-machine to be centered on the piston and aligned with the  $x$ -axis, which is the mean flow direction above the piston during compression. Table 1 summarizes the geometrical parameters and gives an indication of the maximum

variations, measured with a confocal microscope ( $\mu$ surf expert, NanoFocus). Due to the manufacturing process, these variations mostly take place in the streamwise  $x$ -direction.

PIV and particle tracking velocimetry (PTV) was used to measure near-wall velocities. A high-speed Nd : YVO<sub>4</sub> laser (Edgewave IS4II-DE, 532nm) was used to illuminate seeding particles (0.5 $\mu$ m, Dow Corning 510, 50 cSt atomized by Palas AGF 10.0 and Palas UGF 2000 seeders) in a laser sheet (FWHM: 90 $\mu$ m,  $1/e^2$ : 220 $\mu$ m) introduced via the cylinder liner. Contrary to the channel flow, measurements were performed in streamwise and wall-normal  $x$ - $y$ -planes, since optical access to the  $y$ - $z$ -plane is limited by the cylinder head geometry. To measure at crest and valley locations, the measurement plane was shifted slightly out of the central tumble plane. Near-wall velocities reported here are extracted at  $x = 0$  mm and  $-60^\circ$  CA.

The Mie scattering was imaged by a Phantom v2640 high-speed camera with a 180mm Sigma objective. The system was angled towards the piston by  $5^\circ$  to reduce vignetting, while the camera was positioned in an additional Scheimpflug angle of  $9^\circ$ . A magnification of 5.8 (2.3 $\mu$ m/px) was achieved by employing 400mm of distance tubes. Additionally, the astigmatism introduced by the curved cylinder glass was corrected by a  $f=2000$ mm cylindrical lens. To transform the image to a real-world coordinate system and to remove remaining optical distortions, a high-resolution calibration target (LaVision) and polynomial dewarping was employed.

Vector fields were calculated with Davis 10.1.2 (LaVision). A multi-pass procedure with decreasing interrogation window sizes (96 $\times$ 96 px  $\rightarrow$  48 $\times$ 48 px) with 50% overlap was employed. Vector post-processing deleted vectors with a peak ratio smaller than 1.5 and applied a universal outlier detection. A final PIV/PTV processing in Davis 10.0.5 used this vector field to calculate velocities for individual particles. Particle sizes of 1px to 6px, a threshold of 55 counts, a final interrogation window size of 6 $\times$ 6 px and a maximum pixel shift relative to the reference of 3px were set as parameters. No further vector deletion was needed.

The resulting high-resolution, scattered vector data was further processed in Matlab (Mathworks). To improve position accuracy, the vector locations were shifted to the respective mid-vector location. For the flat wall cases, the piston position was determined by the laser reflection on the piston surface and the symmetry axis of mirrored particles on the reflective metal surface. This is not visible in case of the structured surfaces, where laser reflections on characteristic features of the structures were triangulated and related to the flat piston surface. A rectangular grid of 1000  $\times$  20 $\mu$ m<sup>2</sup> was positioned with the edge of the first cell on the piston wall location. Then an average vector was calculated from all vectors in each grid cell. The resulting gridded vector field was phase-averaged over all cycles (per cell 600 to 1200 cycles

with at least one vector). Additionally a moving average filter with kernel size 3 was applied to the vertical velocity component  $V$  to reduce noise.

### 4.3 Results & comparison to turbulent channel flow

The streamwise velocity profiles obtained in the IC engine via PTV during compression at  $-60^\circ$ CA are shown in Fig. 5 on the right, while the corresponding channel flow results (HW and DNS) are shown in the left part of this figure. *Streamwise* denotes the velocity component along the ridge ( $x$ -direction).

The black lines correspond to the reference case with smooth (flat) surfaces for both flows. It can be seen that the velocity boundary layer profiles of these two flows are indeed quite different, as expected. While for turbulent channel flow the expected steep gradient at the wall followed by a logarithmic region (not explicitly visible in the chosen linear scale) is present, the velocity increases more gradually in case of the IC engine, which is known to not exhibit a logarithmic region as outlined by Renaud et al. (2018).

Even though the global bulk Reynolds numbers are of similar magnitude, they correspond to different flow situations: while the channel flow features a developed turbulent flow, the near-wall IC engine flow is unsteady, i.e. the geometry, heat flux and flow field are changing continuously during compression. Furthermore the piston region is subject to different flow conditions during one engine cycle, such as flow separation, impingement and adverse pressure gradients.

The considered boundary layer flow that forms on the piston during compression at  $-60^\circ$ CA can be described unsteady, since it was estimated by Borée and Miles (2014) that turbulent time scales in a logarithmic region would be in the same order of magnitude as the large-scale flow and its turbulence. This difference in the channel and IC engine flow can be further illuminated by comparing the local Reynolds number, which is comparably low for the engine and would correspond to laminar flow conditions in a channel (see the discussion of the present boundary layer parameters in Sect. 4.1). On the other hand the shape factor  $H = \delta_1^*/\delta_2^* \approx 1.7$  indicates a turbulent or transient-regime behaviour (Renaud et al. (2018)).

Besides these differences in flow boundary conditions, the average flow over the piston is wall-parallel, aligned with the surface structures in a broad spanwise region of  $z = 0 \pm 10$  mm from the tumble plane, and no systematic mean flow variation in the streamwise  $x$ -direction at this central piston region is known.

We aim to understand whether the effects induced by ridge-type roughness, which we have seen to be rather insensitive to  $Re_b$  for the channel flow (see Fig. 3), are also present under these complex engine flow conditions.

For the corresponding analysis of the velocity profiles, we treat the ridges as deposition type roughness in the sense that we choose the valley of the ridges as zero location for the wall-normal distance of the velocity profiles. Since the channel half-height  $\delta$  is defined on the net fluid volume in the channel (cf. Sect. 3.1), spanning from the melt-down height of the structured surface to the channel centerline, the approach of measuring wall distance from the ridge valley shifts the location at which  $y/\delta = 1$  is reached slightly off the centerline. This shift is in the order of  $y/\delta \leq 0.015$ . For the present data analysis, the wall distance measured from the ridge valley is always normalized by the boundary-layer thickness of the smooth wall reference case, i.e.  $\delta = 12.60$  mm for the channel and  $\delta_{99} = 0.89$  mm for the engine flow.

The measured velocity profiles are shown in Fig. 5, where the left plots correspond to channel flow data (HW and DNS) and the right plots to the piston boundary layer (PTV). The top row contains data for triangular surface structures, and the bottom row corresponds to rectangular ridges. The black vertical lines indicate the relative height  $h/\delta$  of the ridges in each case which is significantly larger in the engine flow due to the small physical size of the boundary layer as discussed in Sect. 1.

For the triangular ridges (top part of Fig. 5) the most obvious effect is a significant reduction of  $U$  on top of the ridges (blue) for both flow scenarios that is not confined to the ridge vicinity but extends far into the flow. For the engine flow (top right part of Fig. 5) results obtained at two different ridges in the flow separated by  $s = 1.35$  mm are visible. The same panel also includes two black lines describing the smooth wall reference case at slightly different positions: once in the central tumble plane, once 1 mm sideways. These show an excellent reproducibility between different measurements and indicate a negligible spanwise variation of the piston boundary layer. The greater differences visible for the two triangular crest measurements could indicate a stronger off-center change induced by the triangular structures in addition to being measured spatially farther apart. In case of the rectangular ridges, there appears to be a smaller spanwise influence in the engine. For this configuration (Fig. 5 bottom right) measurements above two neighbouring valleys were taken (red lines). These indicate a small variation only, similar to the smooth wall reference case.

The reduced flow velocities on top of the ridges can be interpreted as a wall-normal shift of the U-profiles which is slightly different for the two triangular crest measurements. The vertical black line denotes the wall-normal location of the ridge tip in all plots which clearly corresponds to the location of zero-velocity for the DNS and HW channel flow data. In case of the engine flow such an obvious agreement is not visible, especially for the triangular structures, indicating measurement uncertainties which are higher in the engine

environment. First, the spatial averaging of the laser sheet is likely to increase the apparent velocity, especially above the triangular ridge due to the strong spanwise variations at this location (compare Fig. 3). Adding to the effect of the sheet thickness, the laser sheet  $z$ -position is subject to uncertainty even after careful alignment due to engine vibrations. Finally, the piston surface level determination is less certain on surfaces with structures, therefore the wall distance might be underestimated in this case.

The velocity profiles above crests and valleys collapse at wall-normal distances significantly larger than  $h/\delta$  in all flows. For the two channel flows, this collapse is achieved at wall distances larger than  $y/\delta \approx 0.8$ . This wall distance is similar for the piston boundary layer above triangular ridges but significantly smaller for the flow above rectangular ridges ( $\approx 0.4$ ).

For the piston boundary layer, the wall-normal distance up to which a spanwise inhomogeneity in the streamwise mean velocity is present above the ridge-type roughnesses is roughly in the order of two ridge heights. When scaled with  $h$  the wall-normal extent of the mean flow inhomogeneity is significantly larger for the channel flow. This might be an indication of a comparably smaller effect of the surface structures onto the piston boundary layer caused by, e.g. different turbulence properties of the two boundary layers, the influence of the large scale, turbulent tumble flow on the engine boundary layer, or the limited streamwise length and time for boundary layer development in case of the engine flow. The upstream extent of the structures from the measurement location is 20 mm (22.5 when normalized with  $\delta_{99}$ ). Also, it is noteworthy again that the average near-wall flow is wall parallel for this section but the piston wall's wall-normal movement is still present.

The velocity profiles in the center of the respective valleys between the ridges (red lines) in general show a weaker modification than for the flow above the crests. The general modification of the valley velocity profiles is in qualitative agreement between the two different ridge types, but more pronounced in case of the rectangular ridges. This difference might simply be attributed to the fact that  $s/\delta$  is smaller for rectangular ridges such that the effect that compensates the crest velocity profiles can spread over a wider region in case of the triangular ridges.

However, there is a systematic difference between channel flow and engine flow data for the red curves of Fig. 5. In the channel flow configuration a slight increase in  $U$  above the valleys can be observed for both ridge types whereas the piston boundary layer reveals a clear reduction in  $U$  above the valley of the rectangular ridge which is also present but less pronounced for the triangular ridge. This difference can probably be attributed to the different operating conditions of the two flows. While the channel flow data are compared at the same flow rate (i.e. the same bulk Reynolds number)

the engine flow is driven by the prescribed operating conditions. In order to maintain the same flow rate in the channel flow, an increased streamwise pressure gradient is required to balance the drag increasing effect of the induced ridge-type roughness. Thus, the power added to the channel flow is increased (Hasegawa et al. 2014). The requirement of an identical global flow rate for smooth and rough channels can therefore lead to a local increase in  $U$ . On the contrary, the flow in the engine appears to be best described by similar power being available to drive the flow at the specific operating point such that the increased momentum loss towards the wall due to surface roughness (streamwise ridges in this case) can lead to a reduction in the overall flow rate of the near-wall boundary layer. In consequence we observe a general reduction in  $U$  at both, the crest and the valley of the streamwise ridges for the engine flow.

Overall, the strong spanwise inhomogeneity of the mean streamwise flow field induced by ridge-type roughness in turbulent channel flows is also detected in the boundary layer forming on top of the engine piston during parts of the operation cycle. For the specific ridge-type roughnesses of the present investigation the wall-normal extension of this spanwise inhomogeneity is smaller for the engine if normalized by the ridge height, extending up to approximately twice the ridge height, while extensions beyond five ridge heights are visible for the channel flow configuration.

While the strong spanwise variation of  $U$  that extends well beyond  $h$  can be directly linked to the presence of secondary motions of the Prandtl's second kind in the plane normal to the main flow direction (at least for channel flow), the secondary flow itself becomes accessible through profiles of the wall-normal vertical velocity profiles  $V$  as depicted in Fig. 6. Here, the data for channel and engine flow are combined in one figure for each ridge type. The top part of the figure corresponds to triangular ridges and the lower part to rectangular ones. In case of the engine flow, the piston speed  $V_0$  is subtracted from the measured wall-normal velocity in order to make the data comparable to the channel flow. There was a sufficient number of cycles acquired for converged mean profiles. The remaining ripple can be attributed to artifacts due to the spatial image transformation, which are visible at this fine scale.

The data from the engine experiment clearly show a net upward motion on top of the crest and a net downward motion above the valley, i.e a comparable effect as observed in channel flow of large scale secondary motions. As expected, these vertical mean flow velocities are larger in case of the triangular ridges (Fig. 6, top), which were designed to yield a more intense secondary motion. The confidence interval of the mean (95%) is roughly  $8 \times 10^{-3}$  when normalized by  $U_0$ , which is significantly smaller than the difference between crest and valley profiles in the case of the triangular ridges.

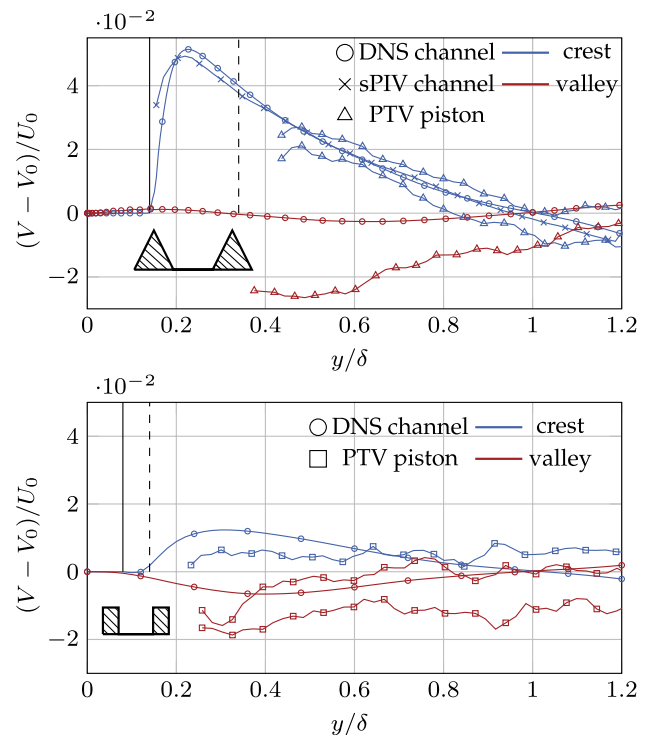


**Fig. 6** Comparison of vertical velocity  $V$  profiles between turbulent channel (DNS and sPIV) and IC engine (PTV—triangular/rectangular markers) for triangular (top) and rectangular (bottom) ridges.  $V_0$  is the measured vertical piston velocity in a piston-relative frame ( $V_0 = 0$  in turbulent channel) and  $\delta$  corresponds to  $\delta_{99}$  for the piston boundary layer. The black vertical lines represent the ridge height  $h/\delta$  (solid line: channel, dashed line: piston) of each case

Figure 6 also includes the vertical velocity for the channel flow configurations obtained with sPIV (triangular ridges) and DNS (both ridge types) in which the net upward and downward motions above crest and valley, respectively, can also be seen. Beyond the fact that the present results provide an indication of the presence of large-scale secondary flow in the engine, the relative upward motion above the crests is in surprisingly good quantitative agreement between the engine and the channel flow for both ridge types. We note that this stunning agreement might be coincidental, as not only the boundary layers but also the ridge structures themselves differ in their details (see table 1).

The fact that the change in valley vertical velocity for the triangular ridges in the IC engine experiment is much stronger compared to the turbulent channel flow is most likely related to the geometrical difference of the employed ridges, which have a much larger relative spacing in case of the turbulent channel-flow configuration ( $s/\delta = 2.16$  instead of  $s/\delta = 1.51$ ). Therefore, the strongly localized upward motion above the crests of the triangular ridges might be compensated by weaker downward motion over a larger spanwise region for the turbulent channel-flow



configuration. In addition, effects of the absolute piston motion might be present, keeping in mind that the data presented in Fig. 6 is a relative upward or downward motion with respect to the reference piston velocity  $V_0$ . Finally, the IC engine flow is likely to be more three dimensional compared to the channel-flow configuration and is statistically unsteady. Nevertheless, two neighbouring ridges show similar results suggesting the assumption of a local quasi 2D behaviour might be applicable.

## 5 Reynolds number dependency of the friction coefficient

In order to introduce the effect of homogeneous surface roughness into full-scale predictive engineering tools for skin-friction drag, the classical velocity profile of wall bounded shear flows is modified in its logarithmic region. The corresponding downward shift of the velocity profile in this region is called the roughness function  $\Delta U^+$ , which is directly related to the equivalent sand grain roughness of a hydrodynamically rough surface (Chung et al. 2021). This equivalent sand grain roughness is a hydraulic property that has to be determined experimentally for each surface by matching the measured drag to the classical Nikuradse or Moody diagram (Nikuradse 1931; Moody 1944).

For spanwise inhomogeneous roughness this classical approach cannot be taken since the flows above such surfaces often do not obey outer-layer similarity (see also Sect. 3.4). Therefore, novel modelling concepts for spanwise irregular rough surfaces have to be developed as outlined by Chung et al. (2021). It was recently demonstrated by Castro et al. (2021) that the spanwise averaged flow field above streamwise aligned ribs can be described with a modified log-law taking into account the increase of wetted surface area. It might thus be possible to predict the global effect of ridge-type roughness onto the spanwise averaged flow field through a prescription of a velocity profile that is tuned to include the Reynolds number dependency of the generated friction drag.

While Vanderwel et al. (2019) demonstrated that secondary motions themselves are rather independent of Reynolds number, as was also confirmed in the present study, very little is known about the Reynolds number dependency of the corresponding friction factor.

As the first step in this direction, we present pressure drop measurements of the turbulent channel flow over ridge type roughness. These results are summarized in a Nikuradse-type plot for streamwise ridges of two different cross sections in Fig. 7. They are plotted along with results obtained with smooth channel walls which agree very well with the well-known Dean correlation (Dean 1978). The measurements show a significant global drag increase for

the turbulent flow along the structured walls compared to the one along smooth walls in the order of 11–15 % over the entire investigated Reynolds number regime, i.e. increasing slightly from 11–13 % at  $Re_b \approx 1 \times 10^4$  up to 13–15 % at  $Re_b \approx 8 \times 10^4$ . Due to the spanwise inhomogeneities of the streamwise mean flow documented in Figs. 3 and 5, there is naturally also a large spanwise variation in wall-shear stress which we now consider from an averaged point of view only.

The results from DNS are also included in Fig. 7 and show generally good agreement with the experimental results despite slightly smaller  $C_f$  values ( $\approx 5\%$  for smooth reference,  $\approx 3\%$  for structured cases). This difference stems from the periodic boundary conditions of the DNS since the side walls of the experiment also contribute to the global friction drag. Due to the higher drag on the structured surfaces the relative importance of the side wall drag is decreased for these cases.

The observed increase in friction drag is slightly larger for triangular ridges, which is in agreement with the assumption that a larger friction increase is found for stronger secondary motions (Türk et al. 2014; von Deyn et al. 2020; Medjnoun et al. 2020). Note that the increase in wetted surface area compared to the smooth wall reference case is larger for the rectangular ridges (11.7%) than for the triangular ones (6.7%) and thus does not appear to primarily govern the measured drag increase.

For both ridge configurations the  $C_f$  vs  $Re_b$  plot shows a similar trend than the well-known smooth wall correlation. In particular,  $C_f$  decreases monotonically with  $Re_b$ , while classical rough surfaces exhibit a friction factor that eventually becomes independent of  $Re_b$  (Nikuradse 1931). This fully-rough behavior is not existent for the present ridge type roughness.

Considering the 2D-type shape of the investigated structures which do not induce any pressure drag, this absence of a fully-rough behaviour may be expected. We note that the present results agree well with what has been observed

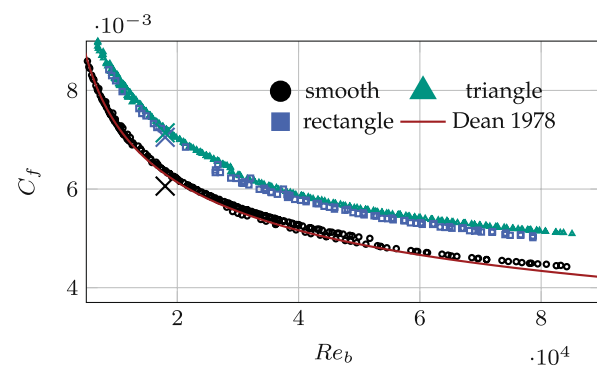


**Fig. 7**  $C_f$  vs.  $Re_b$  obtained in turbulent channel flow.  $C_f$  obtained from DNS included as large crosses. Correlation proposed by Dean (1978) included for reference

for riblets in their drag increasing regime by Gatti et al. (2020). These results indicate that an equivalent sand grain roughness, whose definition relies on an eventually Reynolds number independent friction coefficient, cannot be determined for ridge-type roughness. However, we further note that the observed smooth-wall-like behavior of the friction coefficient bears a resemblance with the results presented by Castro et al. (2021). They show that the spanwise averaged mean velocity profile for a ribbed channel can be predicted with a log-law profile if geometrical features of the ridged channel, in particular the increase in wetted surface area and the decrease in cross-sectional area, are accounted for. These are the ingredients of the well-known hydraulic diameter concept classically utilised for describing the friction factor in straight ducts with complex cross section. As already noted in respect to large riblets by Gatti et al. (2020), the classical (empirical) hydraulic diameter argument, however, underestimates the presently observed drag increase. Therefore, improved definitions of an 'effective duct diameter' for ribbed channels might be one option towards novel predictive tools for these particular internal flows.

Finally, one has to keep in mind that the investigated ridge-type roughness, where smooth streamwise ridges represent roughness strips, has been introduced as a model for realistic spanwise inhomogeneous roughness. Streamwise strips of realistic roughness will induce pressure drag and the question under which flow conditions such surfaces reach a fully rough state and thus a Reynolds number independent friction coefficient remains to be answered in the future investigations.

## 6 Summary and conclusions

The turbulent flow field above ridge-type roughness is investigated in turbulent channel and an IC engine flow. Two types of ridges are considered. First, rectangular ridges which are the most widely investigated ridge types and second, triangular ridges which are known to introduce stronger secondary motions.

For the turbulent channel flow, the generated secondary motions of the Prandtl's second kind were experimentally detected via sPIV and hot-wire anemometry in a channel of aspect ratio 1:12. The measured secondary flow as well as its impact on the streamwise flow field are in very good agreement with IBM based DNS results. This implies that neither the aspect ratio of the experiment nor the IBM approach in the DNS is critical for the set-up. From an experimental point of view the present data shows that the turbulent cross-plane motion can be resolved with sPIV despite the almost two orders of magnitude smaller secondary motion magnitude ( $\approx 4\%$ ) with respect to the streamwise velocity  $U$ . In agreement with the previous literature results

(Vanderwel et al. 2019), the secondary motions show a very weak dependence on Reynolds number. The two ridge configuration investigated in the turbulent channel flow were transferred to the piston of the optically accessible Darmstadt Engine. Within the operating cycle of this four stroke engine, a boundary layer along the piston wall is established during the compression stroke (Renaud et al. 2018). As discussed in Sect. 3.2 this turbulent boundary layer (with a boundary-layer thickness  $\delta_{99} \approx 1$  mm) differs from classical equilibrium boundary layers of wall-bounded shear flows. The present study aimed to investigate whether the formation of secondary flows over ridge type roughness also occurs under these transient and complex flow conditions.

Both ridge type geometries were added to the piston such that they are oriented into the mean flow direction of the piston boundary layer. A laser light sheet was placed in the streamwise wall-normal plane located either on top of a ridge crest or above a valley between two ridges. Using particle tracking velocimetry (PTV) the streamwise and wall-normal velocity components were thus measured in the near-wall region. A significant difference of the wall-parallel (streamwise) mean flow above valleys and crests of the ridges was identified which extends well above the ridge height. This detected spanwise variation of the streamwise mean flow is in reasonable agreement with results obtained in the channel flow configuration for ridge type roughness. The wall-normal velocity component relative to the upward moving piston clearly indicates upwelling motion above the ridge crests and downwelling motion above the valleys which is in agreement with the observations for channel and zero pressure gradient boundary layer flows over ridge-type roughness, documented in literature as well as in the present study. These indicators for the presence of large-scale secondary motions are stronger for the triangular ridges which is also in agreement with the observations in canonical boundary layers that these types of ridges induce stronger secondary flows.

Overall, indications for the presence of large-scale secondary motions in the piston boundary layer are clearly found. The secondary motions in the engine flow appear to have a smaller relative impact on the boundary layer in the sense that first, the triangular structures, which are larger in terms of  $h/\delta$  for the engine test case, result in similar upwelling motions above the crests as observed in the channel flow and that second, the wall-normal extend of the induced spanwise inhomogeneity of the streamwise flow field appears to be smaller for the rectangular structures in the engine (judging from the first-order velocity statistics). This might be related to the different nature of the turbulent boundary layers, where the piston boundary layer turbulence is less shear driven with strong influences of the surrounding complex flow. In addition, the piston boundary layer is of transient nature and the boundary layer has

a limited development length over the ridge-type surface roughness. The fact that indications of secondary motions or their footprints are clearly detected in the engine flow above a ridge-type roughness on the engine piston indicates a remarkable robustness of this flow phenomena in agreement with previous findings (Mejia-Alvarez and Christensen 2013; Womack et al. 2019). This suggests that the occurrence of secondary flows of the Prandtl's second kind above heterogeneous rough surfaces might be a relevant building block of complex flow scenarios.

From a global perspective, the drag increasing nature of ridge-type roughness which leads to an increased pressure drop in a channel flow at constant bulk Reynolds number, manifests itself through a reduced near-wall volume flow rate inside the piston boundary layer. How the presence of secondary motions in combination with an increased boundary-layer displacement thickness influence the near-wall heat transfer, flame quenching in combustion systems and the overall effect on the thermal load of components in technical applications, remains to be investigated in future studies.

Full-scale predictions of drag and heat transfer for turbulent flows over rough walls rely on the use of roughness functions that are directly related to an equivalent sandgrain roughness. For spanwise inhomogeneous rough surfaces, their lack of outer-layer similarity permits the use of this approach (Chung et al. 2021). In addition, the present results show that the investigated ridge-type roughness does not reach a  $Re_b$  independent friction factor such that an equivalent sandgrain roughness cannot be defined. While the observed behavior for  $C_f$ , following the smooth wall curve almost parallelly, suggests the use of a hydraulic diameter concept, the increase in wetted surface area does not primarily govern the drag increase. Future modelling efforts will thus have to include the drag-increasing effects of the secondary motions as well.

**Acknowledgements** We kindly acknowledge the financial support of the Deutsche Forschungsgemeinschaft (DFG, German Research Foundation) through projects 316200959 (Priority Programme 1881) and 237267381-TRR 150 (SFB-Transregio 150). M. Hehner and J. Serpieri are thanked for their support in conducting the sPIV experiments. The numerical part of this work was performed on the supercomputer ForHLR and the storage facility LSDF funded by the Ministry of Science, Research and the Arts Baden-Württemberg and by the Federal Ministry of Education and Research.

**Funding** Open Access funding enabled and organized by Projekt DEAL.

**Open Access** This article is licensed under a Creative Commons Attribution 4.0 International License, which permits use, sharing, adaptation, distribution and reproduction in any medium or format, as long as you give appropriate credit to the original author(s) and the source, provide a link to the Creative Commons licence, and indicate if changes were made. The images or other third party material in this article are included in the article's Creative Commons licence, unless indicated

otherwise in a credit line to the material. If material is not included in the article's Creative Commons licence and your intended use is not permitted by statutory regulation or exceeds the permitted use, you will need to obtain permission directly from the copyright holder. To view a copy of this licence, visit <http://creativecommons.org/licenses/by/4.0/>.

## References

- Alharbi AY, Sick V (2010) Investigation of boundary layers in internal combustion engines using a hybrid algorithm of high speed micro-PIV and PTV. *Exp Fluids* 49(4):949–959. <https://doi.org/10.1007/s00348-010-0870-8>
- Anderson W, Barros JM, Christensen KT, Awasthi A (2015) Numerical and experimental study of mechanisms responsible for turbulent secondary flows in boundary layer flows over spanwise heterogeneous roughness. *J Fluid Mech* 768:316–347. <https://doi.org/10.1017/jfm.2015.91>
- Baum E, Peterson B, Böhm B, Dreizler A (2014) On the validation of LES applied to internal combustion engine flows: part I: comprehensive experimental database. *Flow Turbul Combust* 92(1):269–297. <https://doi.org/10.1007/s10494-013-9468-6>
- Bons JP (2002) St and cf augmentation for real turbine roughness with elevated freestream turbulence. *J Turbomach* 124(4):632–644. <https://doi.org/10.1115/1.1505851>
- Bons JP, Taylor RP, McClain ST, Rivir RB (2001) The many faces of turbine surface roughness. *J Turbomach* 123(4):739–748. <https://doi.org/10.1115/1.1400115>
- Borée J, Miles PC (2014) In-cylinder flow. *Encycl Automot Eng*. <https://doi.org/10.1002/9781118354179.auto119>
- Castro IP, Kim JW, Stroh A, Lim HC (2021) Channel flow with large longitudinal ribs. *J Fluid Mech*. <https://doi.org/10.1017/jfm.2021.110>
- Chevalier M, Schlatter P, Lundbladh A, Henningson DS (2007) SIMSON: a pseudo-spectral solver for incompressible boundary layer flows. *Mekanik, Kungliga Tekniska högskolan, Stockholm*, <http://citeseerx.ist.psu.edu/viewdoc/summary?doi=10.1.1.713.2088>
- Chung D, Monty JP, Hutchins N (2018) Similarity and structure of wall turbulence with lateral wall shear stress variations. *J Fluid Mech* 847:591–613. <https://doi.org/10.1017/jfm.2018.336>
- Chung D, Hutchins N, Schultz MP, Flack KA (2021) Predicting the drag of rough surfaces. *Annu Rev Fluid Mech* 53(1):439–471. <https://doi.org/10.1146/annurev-fluid-062520-115127>
- Colombini M, Parker G (1995) Longitudinal streaks. *J Fluid Mech* 304:161–183. <https://doi.org/10.1017/S0022112095004381>
- Dean RB (1978) Reynolds number dependence of skin friction and other bulk flow variables in two-dimensional rectangular duct flow. *J Fluids Eng* 100(2):215–223. <https://doi.org/10.1115/1.3448633>
- Forooghi P, Stroh A, Magagnato F, Jakirlić S, Frohnappfel B (2017) Toward a universal roughness correlation. *J. Fluids Eng*. 10(1115/1):4037280
- Forooghi P, Stroh A, Schlatter P, Frohnappfel B (2018) Direct numerical simulation of flow over dissimilar, randomly distributed roughness elements: a systematic study on the effect of surface morphology on turbulence. *Phys. Rev. Fluids* 3(4):044605. <https://doi.org/10.1103/PhysRevFluids.3.044605>
- Freudenhammer D, Peterson B, Ding CP, Boehm B, Grundmann S (2015) The influence of cylinder head geometry variations on the volumetric intake flow captured by magnetic resonance velocimetry. *SAE Int J Engines* 8(4):1826–1836. <https://doi.org/10.4271/2015-01-1697>

- Gatti D, von Deyn L, Forooghi P, Frohnappel B (2020) Do riblets exhibit fully rough behaviour? *Exp Fluids* 61(3):81. <https://doi.org/10.1007/s00348-020-2921-0>
- Goldstein D, Handler R, Sirovich L (1993) Modeling a no-slip flow boundary with an external force field. *J Comput Phys* 105(2):354–366. <https://doi.org/10.1006/jcph.1993.1081>
- Güttler A (2015) High accuracy determination of skin friction differences in an air channel flow based on pressure drop measurements. KIT Scientific Publishing, Germany
- Hasegawa Y, Quadrio M, Frohnappel B (2014) Numerical simulation of turbulent duct flows with constant power input. *J Fluid Mech* 750:191–209. <https://doi.org/10.1017/jfm.2014.269>
- Hehner M, Gatti D, Mattern P, Kotsonis M, Kriegseis J (2021a) Beat-frequency-operated dielectric-barrier discharge plasma actuators for virtual wall oscillations. *AIAA J* 59(2):763–767. <https://doi.org/10.2514/1.J059802>
- Hehner MT, von Deyn LH, Serpieri J, Pasch S, Reinheimer T, Gatti D, Frohnappel B, Kriegseis J (2021b) Stereo piv of oscillatory plasma discharges in the cross plane of a channel flow. 14th International Symposium on Particle Image Velocimetry (ISPIV 2021), August 1–5, 2021 <https://doi.org/10.18409/ispiv.v1i1.117>
- Hinze JO (1967) Secondary currents in wall turbulence. *Phys Fluids* 10(9):S122–S125. <https://doi.org/10.1063/1.1762429>
- Hutchins N, Nickels TB, Marusic I, Chong MS (2009) Hot-wire spatial resolution issues in wall-bounded turbulence. *J Fluid Mech* 635:103–136. <https://doi.org/10.1017/S0022112009007721>
- Hwang HG, Lee JH (2018) Secondary flows in turbulent boundary layers over longitudinal surface roughness. *Phys Rev Fluids* 3(1):014608. <https://doi.org/10.1103/PhysRevFluids.3.014608>
- Jainski C, Lu L, Dreizler A, Sick V (2012) High-speed micro particle image velocimetry studies of boundary-layer flows in a direct-injection engine. *Int J Engine Res* 14(3):247–259. <https://doi.org/10.1177/1468087412455746>
- Luchini P (2018) Structure and interpolation of the turbulent velocity profile in parallel flow. *Eur J Mech B Fluids* 71:15–34. <https://doi.org/10.1016/j.euromechflu.2018.03.006>
- Ma PC, Ewan T, Jainski C, Lu L, Dreizler A, Sick V, Ihme M (2016) Development and analysis of wall models for internal combustion engine simulations using high-speed micro-PIV measurements. *Flow Turbul Combust* 98(1):283–309. <https://doi.org/10.1007/s10494-016-9734-5>
- MacDonald JR, Fajardo CM, Greene M, Reuss D, Sick V (2017) Two-point spatial velocity correlations in the near-wall region of a reciprocating internal combustion engine. *SAE Int.* <https://doi.org/10.4271/2017-01-0613>
- Medjnoun T, Vanderwel C, Ganapathisubramani B (2018) Characteristics of turbulent boundary layers over smooth surfaces with spanwise heterogeneities. *J Fluid Mech* 838:516–543. <https://doi.org/10.1017/jfm.2017.849>
- Medjnoun T, Vanderwel C, Ganapathisubramani B (2020) Effects of heterogeneous surface geometry on secondary flows in turbulent boundary layers. *J Fluid Mech* 886:A31. <https://doi.org/10.1017/jfm.2019.1014>
- Mejia-Alvarez R, Christensen KT (2013) Wall-parallel stereo particle-image velocimetry measurements in the roughness sublayer of turbulent flow overlying highly irregular roughness. *Phys Fluids* 25(11):115109. <https://doi.org/10.1063/1.4832377>
- Moody LF (1944) Friction factor for pipe flow. *Trans ASME* pp 671–684
- Nikuradse J (1931) Strömungswiderstand in rauhen Röhren. *ZAMM J Appl Math Mech / Zeitschrift für Angewandte Mathematik und Mechanik* 11(6):409–411. <https://doi.org/10.1002/zamm.19310110603>
- Örlü R, Vinuesa R (2017) Thermal anemometry. *Exp Aerodyn.* <https://doi.org/10.1201/9781315371733>
- Örlü R, Fransson JHM, Henrik Alfredsson P (2010) On near wall measurements of wall bounded flows—The necessity of an accurate determination of the wall position. *Prog Aerosp Sci* 46(8):353–387. <https://doi.org/10.1016/j.paerosci.2010.04.002>
- Renaud A, Ding CP, Jakirlic S, Dreizler A, Böhm B (2018) Experimental characterization of the velocity boundary layer in a motored IC engine. *Int J Heat Fluid Flow* 71:366–377. <https://doi.org/10.1016/j.ijheatfluidflow.2018.04.014>
- Schmitt M, Frouzakis CE, Wright YM, Tomboulides AG, Boulouchos K (2015) Direct numerical simulation of the compression stroke under engine-relevant conditions: evolution of the velocity and thermal boundary layers. *Int J Heat Mass Transf* 91:948–960. <https://doi.org/10.1016/j.ijheatmasstransfer.2015.08.031>
- Shimura M, Yoshida S, Osawa K, Minamoto Y, Yokomori T, Iwamoto K, Tanahashi M, Kosaka H (2018) Micro particle image velocimetry investigation of near-wall behaviors of tumble enhanced flow in an internal combustion engine. *Int J Engine Res* 20(7):718–725. <https://doi.org/10.1177/1468087418774710>
- Stroh A, Schafer K, Forooghi P, Frohnappel B (2019) Secondary flow and heat transfer in turbulent flow over streamwise ridges. *Int J Heat Fluid Flow* 885:31. <https://doi.org/10.1016/j.ijheatfluidflow.2019.108518>
- Stroh A, Schäfer K, Frohnappel B, Forooghi P (2020) Rearrangement of secondary flow over spanwise heterogeneous roughness. *J Fluid Mech.* <https://doi.org/10.1017/jfm.2019.1030>
- Türk S, Daschiel G, Stroh A, Hasegawa Y, Frohnappel B (2014) Turbulent flow over superhydrophobic surfaces with streamwise grooves. *J Fluid Mech* 747:186–217. <https://doi.org/10.1017/jfm.2014.137>
- Vanderwel C, Ganapathisubramani B (2015) Effects of spanwise spacing on large-scale secondary flows in rough-wall turbulent boundary layers. *J Fluid Mech.* <https://doi.org/10.1017/jfm.2015.292>
- Vanderwel C, Stroh A, Kriegseis J, Frohnappel B, Ganapathisubramani B (2019) The instantaneous structure of secondary flows in turbulent boundary layers. *J Fluid Mech* 862:845–870. <https://doi.org/10.1017/jfm.2018.955>
- von Deyn LH, Gatti D, Frohnappel B, Stroh A (2020) Parametric study on ridges inducing secondary motions in turbulent channel flow. *PAMM.* <https://doi.org/10.1002/pamm.202000139>
- Wangawijaya DD, Baidya R, Chung D, Marusic I, Hutchins N (2020) The effect of spanwise wavelength of surface heterogeneity on turbulent secondary flows. *J Fluid Mech.* <https://doi.org/10.1017/jfm.2020.262>
- Westerweel J, Scarano F (2005) Universal outlier detection for piv data. *Exp Fluids* 39(6):1096–1100. <https://doi.org/10.1007/s00348-005-0016-6>
- Womack KM, Schultz MP, Meneveau C (2019) Outer-layer differences in boundary layer flow over surfaces with regular and random arrangements. 11th International Symposium on Turbulence and Shear Flow Phenomena (TSFP11), Southampton, UK
- Yang J, Anderson W (2018) Numerical study of turbulent channel flow over surfaces with variable spanwise heterogeneities: topographically-driven secondary flows affect outer-layer similarity of turbulent length scales. *Flow Turbul Combust* 100(1):1–17. <https://doi.org/10.1007/s10494-017-9839-5>
- Zampiron A, Cameron S, Nikora V (2020) Secondary currents and very-large-scale motions in open-channel flow over streamwise ridges. *J Fluid Mech.* <https://doi.org/10.1017/jfm.2020.8>

**Publisher's Note** Springer Nature remains neutral with regard to jurisdictional claims in published maps and institutional affiliations.